Journal of The Electrochemical Society, 2024 **171** 100518

Influence of Conductive Additives and Binder on the Impedance of Lithium-Ion Battery Electrodes: Effect of an Inhomogeneous Distribution

Mrudula Prasad,[1,2] Simon Hein,[1,2] Timo Danner,[1,2,z] Benedikt Prifling,[3] Rares Scurtu,[4] Alice Hoffmann,[4] André Hilger,[5] Markus Osenberg,[5] Ingo Manke,[5] Margret Wohlfahrt-Mehrens,[4] Volker Schmidt,[3] and Arnulf Latz[1,2,6]

[1]*German Aerospace Center (DLR), Institute of Engineering Thermodynamics, 70569 Stuttgart, Germany*
[2]*Helmholtz-Institut Ulm für Elektrochemische Energiespeicherung (HIU), 89081 Ulm, Germany*
[3]*Ulm University (UUlm), Institute of Stochastics, 89081 Ulm, Germany*
[4]*ZSW-Zentrum für Sonnenenergie- und Wasserstoff-Forschung Baden-Württemberg, 89081 Ulm, Germany*
[5]*Helmholtz-Zentrum Berlin für Materialien und Energie, 14109 Berlin, Germany*
[6]*Ulm University (UUlm), Institute of Electrochemistry, 89081 Ulm, Germany*

The conductive additive and binder domain (CBD) is an essential component of lithium-ion battery electrodes. It enhances the electrical connectivity and mechanical stability within the solid electrode matrix. Migration of the binder during electrode drying can lead to an inhomogeneous distribution of the CBD, impeding transport of lithium ions into the electrodes, and diminishing the electronic pathways between solid particles and the current collector. This is especially prominent in thick electrodes at high drying rates. Therefore, we investigate the effect of a non-uniform CBD distribution on the electrochemical performance of NMC622 electrodes via microstructure-resolved three-dimensional (3D) simulations on virtual electrodes, based on tomographic image data, and compare them with experimental results. The valuable information derived by combining microstructure-resolved models with electrochemical impedance spectroscopy measurements on symmetric cells under blocking electrolyte conditions is used to characterize the lithium-ion transport in the electrode pore space, including the contributions of the CBD. The effect of this inhomogeneity on electrode performance is then gauged via galvanostatic discharge simulations under changing discharge currents and for varying electrode densities. Through our work, we demonstrate the significance of the CBD distribution and enable predictive simulations for future battery design.
 [DOI: 10.1149/1945-7111/ad81b9]

Manuscript submitted August 6, 2024; revised manuscript received September 23, 2024. Published October 18, 2024.

Supplementary material for this article is available online

Lithium-ion batteries are the dominant power source for mobile applications ranging from portable electronic devices to electric vehicles. Especially in the automotive sector, the demand for improved batteries with high energy density and reduced cost is increasing tremendously. Advances in these two properties are generally seen as a prerequisite to promote the breakthrough of battery electric vehicles. One route toward these targets is the development of cells consisting of electrodes with high areal loading.[1–4] This concept allows to save on passive materials and additionally, has the potential to save processing time during cell assembly. The passive materials in a lithium-ion battery cathode are the conductive carbon, assisting in improving the electronic conductivity of the electrode owing to the low electronic conductivity of the active material (AM),[5] and the polymeric binder, which forms a cohesive web encompassing the cathode materials and adheres them to the current collector (CC).[6,7] The carbon black and polymeric binder is assumed to form a composite homogeneous phase with an inherent nanoporosity, referred to as the carbon-binder domain (CBD). This is further encouraged by the high-surface area of the carbon black. However, an intrinsic issue of an electrode with high areal loading is longer transport pathways in the electrode and electrolyte, which reduce the power density of the cells. The presence of CBD results in short-chain intra-CBD, and long-chain AM-CBD electronic conduction networks, as well as tortuous ion transport pathways.[8] At high currents mostly transport limitations in the electrolyte become prominent and reduce the performance of the cell.[9,10] Several concepts are suggested in the literature in order to improve the transport in the electrolyte.[7,11] Additionally, due to the high areal loading, new challenges arise in the processing of the electrodes, such as during the mixing, drying and calendering steps. Especially for thick electrodes it has been shown that an unfavourable CBD structure, resulting from features of the mixing process, decisively impairs their industrially required roll-to-roll processability.[12–15] A production step that plays a critical role on the final electrode backbone structure is, the drying process. Nikpour et al. adeptly summarise prior literature on electrode drying, and show experimentally the evolution of the electrode microstructure during this process.[16] Hence, when high drying rates are applied, this composite phase migrates conjointly toward the surface of the electrode due to drag of the evaporating solvent, and the resulting capillaryforces.[16–18] This phenomenon causes an inhomogeneous distribution of the CBD from current collector to separator; an effect that is exacerbated in thicker electrodes. As an outcome of this process, the electrodes experience: i) a depletion of CBD at the current collector deteriorating electronic pathways and the adhesion of the electrode layer, and ii) accumulation of the CBD at the electrode surface blocking pathways for electrolyte transport.[7] Both effects have a negative effect on the performance of the electrode. The drying time-scale considered is much shorter than the redistribution time of the AM, hence the convective flow does not effect the AM backbone structure.

Several articles[19–30] demonstrate that electrochemical impedance spectroscopy (EIS) measurements on symmetrical cells are a very useful tool for the characterization of lithium-ion transport in the electrode pore space. Similar EIS measurements in the same setup as in this study have been reported for thinner electrodes. Under ideal conditions (uniform electronic and ionic conductivities across the electrode), a linear increase of the imaginary part in a 45 degree angle to the real axis[31,32] is expected. However, for thicker electrodes, the presence of a high-frequency semi-circle for experiments conducted under blocking electrolyte conditions[27,33] was noted. These semi-

[z]E-mail: timo.danner@dlr.de

circles were witnessed at frequencies higher than the charge-transfer resistance. Amongst some of the origins for this, the following have been highlighted in the literature: (i) the contact resistance between the electrode material and the CC metal,[34] (ii) heterogeneity within the meso- and microporous space of an electrode,[35] and (iii) inhomogeneities in the macroscale distribution of the passive and active materials.[27] These origins coincide with the effects of applying a high drying rate.[17] In the literature, there are reports that focus on the influence of the CBD and its volume fraction on battery operation,[5,36–42] on the formation of the conductive networks,[19,43] and on the effective properties of the CBD itself.[44–47] In most studies, a combination of imaging techniques and electrochemical characterization is used to evaluate the distribution of active particles, and a resistor network is used to model the electrochemistry. Zielke et al. use transport simulations on a combination of electrodes reconstructed from focused ion beam scanning electron microscopy (FIB-SEM) tomography and virtually generated electrodes in order to enrich the information content of the experimental studies.[48] A similar approach is also described in Ref. 37. In the majority of the studies, the focus lies on the distribution of the CBD in the bulk of the electrodes,[33] with a focus on the anode side.[41,49] An analysis of the effect of an inhomogeneous distribution across the electrode thickness using symmetrical impedance spectroscopy is provided in Ref. 27. However, a study which includes physics-informed microstructure-resolved electrochemical simulations in order to provide a more quantitative analysis of the effect on the cathode side could not be found in the literature. Hence, in this work, we attempt to deconvolute the rationality for this unanticipated high-frequency slope by conducting physics-based microstructure-resolved 3D simulations and validating them against experiments. Our model inherently considers the local inhomogeneities in the electrode, as well as the morphology and distribution of the electrode materials.[50–53] This allows the transport processes of the electrolyte within the AM and CBD to be resolved, depending on the local lithium-ion concentration. We could demonstrate that symmetric impedances can be used to deduce the morphology and distribution of the CBD within the electrode. In combination with microstructure-resolved simulations, this approach was able to provide a quantitative link between CBD properties and half-cell performance for beyond state-of-the-art electrodes with an areal capacity of above 7 mAh/cm^2.

In Experimental Methods section, we provide a description of the manufacture as well as a structural and electrochemical characterization of the electrodes. Three different cathodes each with varying electrode densities (2.7, 3.0, and 3.3 g cm^{-3}) and a similar mass loading of 43.6 mg/cm^2 are characterized by synchrotron tomography. The CBD distribution cannot be resolved in the tomography data due to a low contrast to the pore space, hence, we additionally collect EDX-spectra on a cross-cut of the electrode for a qualitative analysis of the CBD distribution in the bulk of the electrode. We then iteratively add the effects of binder migration to the virtual electrodes based on its agreement to the experimental EIS data. A description of this procedure is given in Simulative methods section. Half-cell (HC) discharge simulations are run on the same set of electrodes and are availed to corroborate the findings from impedance simulations (see Results and discussion section). Finally, in Summary and conclusions section, we summarise our findings.

Experimental Methods

Electrode preparation and cell assembly.—For the preparation of the composite positive electrodes, a suspension of the active material $LiNi_{0.6}Co_{0.2}Mn_{0.2}O_2$ (NMC622 BASF), conductive additives and polyvinylidene fluoride binder (PVDF, Solvay Solexis) in the weight ratio 93:3:4 was prepared in the solvent N-methylpyrrolidone (NMP, Sigma Aldrich). The ratio of the conductive additives carbon black (Super P Li) to graphite (C-NERGY SFG 6 L) from Imerys (formerly Timcal) was chosen 2:1 for the reasons described in previous work.[1] For the preparation of the suspension, the solid components were added to a 1.7 dm^3 planetary mixer (Grieser, Germany) equipped with a cross bar stirrer (CS) and a butterfly stirrer (BS) and dry-mixed for 10 min before the first portion of the solvent was added. The mixture was kneaded for 20 minutes within a temperature range of 48 °C to 62 °C and at a rotational speed of 67 rpm and 506 rpm of the CS and BS, respectively, to result in a total solid content of 88.7 wt.-%. Further NMP was added in three portions and after each addition, a rotational speed of 88 rpm (CS) and 900 rpm (BS) was applied over a total period of 4.5 hours. This period can be subdivided into a second kneading phase of a duration of 1.5 hours at a solid content of 85 wt.-% and a following diluting phase. The final solid content was 74.9 wt.-%.The suspension was applied with a doctor blade (Elcometer, Germany) on a 20 μm thick aluminum collector foil (Korff AG, Switzerland) fixed by a vacuum plate and the fim was dried on a heat plate. The average mass loading was 43.3 mg cm^{-2}. The electrode was calendered with a table calender (Sumet, Germany) to different densities of the composite of 2.8, 3.0, and 3.3 g cm^{-3}, respectively. From these electrodes samples, circular discs with a diameter of 1.2 cm corresponding to an area of 1.13 cm^2 were punched and thoroughly dried for 16 h at 130 °C under vacuum. For the preparation of half cells in an argon-filled glove box, they were mounted in 2016-type coin cells as working electrodes and combined with lithium foil as a counter electrode, glass microfibre (GF/A, Whatman) as a separator and 1.0 M $LiPF_6$ in a mixture of ethylene carbonate and ethylmethyl carbonate (ratio 3:7 by weight) with an additional 2 wt.-% of vinylene carbonate (BASF) as electrolyte. For impedance measurements, symmetrical 2016-type coin cells were assembled in the same way and with the same materials as described for the half-cells apart from the following deviation. As electrodes, two discs from the same electrode sample, one with a diameter of 1.2 cm and the other with a diameter of 1.6 cm, were used. The difference in diameter was chosen to ensure complete overlapping of the smaller electrode by the larger one.

Structural characterization.—The microstructure-resolved simulations for the calculation of electrochemical impedance spectra will be performed on the tomographic image data of those electrodes described in Electrode preparation and cell assembly section. Tomographic imaging was performed at the synchrotron X-ray facility BAMline (BESSYII, Berlin, Germany).[54] A monochromatic X-ray beam was produced by a Si-W multilayer monochromator. The energy was 25 keV and an energy resolution of $\Delta E/E=10^{-2}$ was applied. The X-rays were converted into visible light using a cadmium tungstate scintillator screen. The field of view covered by the optical lens system in combination with a CCD-camera (PCO camera, 4008×2672 pixels) was 1.8 × 1.2 mm^2. With an exposure time of 2.5 seconds, 2200 projections were measured over an angular range of 180°. The size of a voxel in the reconstructed image is 438 nm. After reconstruction, a 16-bit grayscale image of the electrode was created. In order to perform the electrochemical simulations, a binarization of the image data is necessary, i.e. the grayscale image has to be transformed into a binary image, where one phase shows the active material particles, and the other phase the union of pores, binder and additives. Note that, due to the low contrast, it is not possible to differentiate between the CBD and pore space, therefore, it will be added on a model basis later (see Generation of virtual electrodes section). The binarization was done by global thresholding, i.e. every voxel with a value larger than the assigned threshold is allocated to the active material particles, and the remaining voxels to the CBD and pore space. The threshold is chosen such that the volume fraction of the active material calculated from the binarised image matches the volume fraction determined from the weight ratio of the materials, their bulk densities and the density of the electrode, which results in 57.4 vol.-%. A 3D rendering of the resulting binarized image data is shown in Fig. 1d.

Cross-sections of electrodes were generated by broad-beam argon ion milling (Hitachi IM4000Plus). Milling time was at least

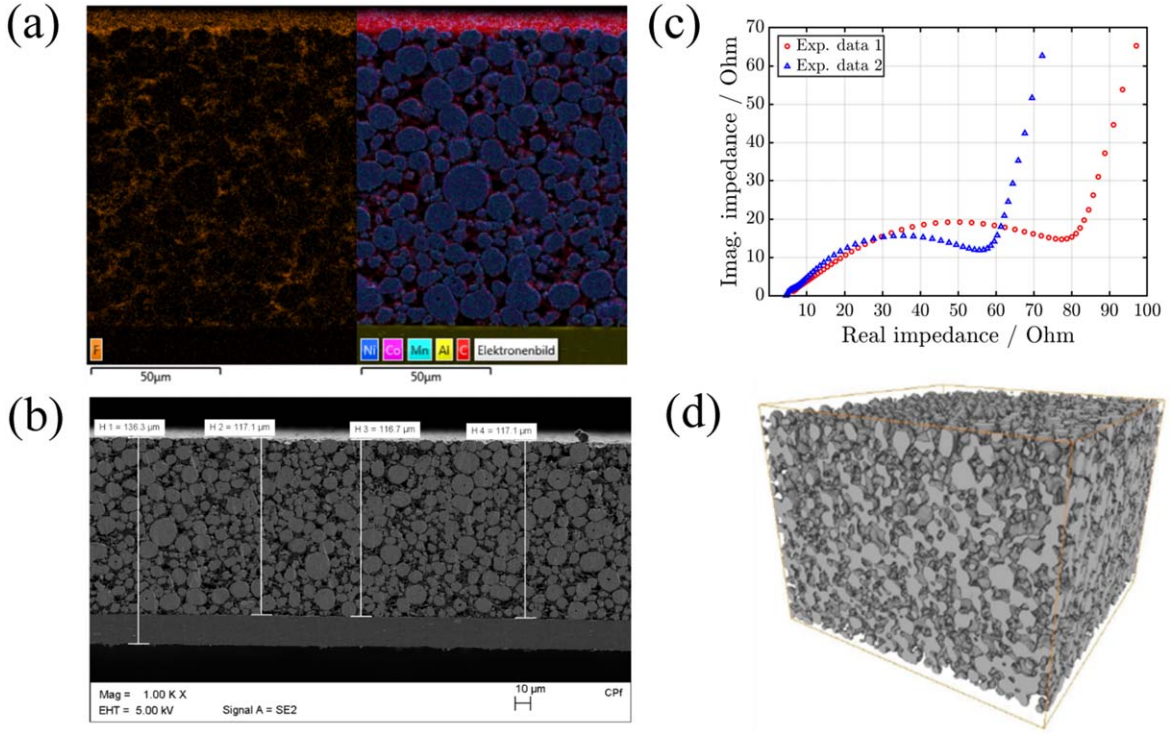

Figure 1. Segment (a) and (b) show SEM images of a cross-cut through an electrode with an areal capacity of 5.7 mAh/cm^2 and a density of 3.0 g cm^{-3}. (a) Includes in false-color, information of EDX spectra representing different elements present in the cathode. (b) includes thickness measurements for the electrode coating and current collector. Impedance spectra measured in a symmetric cell setup under blocking electrolyte conditions for the electrodes with the same density and an areal capacity of 7.3 mAh/cm^2 are given in (c), and a cutout of the binarized tomographic image data without CBD are presented in (d). Note: segments (a) and (b) are included for visual corroboration.

2 h at an ion beam voltage of 5 kV. Scanning Electron Microscopy (SEM) and energy dispersive X-ray spectroscopy mapping (EDX) was carried out using a LEO 1530 VP microscope equipped with a Gemini thermal field emission column to investigate the morphology and the elemental distribution of the electrodes. SEM images were obtained with a secondary electron detector at accelerating voltages between 4 and 5 kV. Fluorine was used as tracing element for the presence of the PVDF binder. Due to the sample heterogeneity, EDX is not perfectly suited to determine absolute concentrations of certain elements, however, observation of relative changes of the count rate under constant conditions has turned out to be a feasible method for gathering reliable information.[17] Nevertheless, the absolute values strongly depend on the measuring parameters and therefore this technique only allows a qualitative interpretation.

Electrochemical characterization.—The galvanostatic tests were performed with a cell test system from BaSyTech GmbH (Germany). After assembling, the cells were allowed to rest for 24 hours. They were then formed by three consecutive, galvanostatic symmetric cycles at C/10 between 3.0 and 4.3 V. Subsequently, their discharge rate capability was investigated by consecutively executing three half cycles between 4.3 V and 3.0 V at a current density of 1 mA cm^{-2}, 3 mA cm^{-2}, 6 mA cm^{-2}, 8 mA cm^{-2}, 10 mA cm^{-2} and 12 mA cm^{-2}, respectively. After the discharge with 6, 8 and 10 mA cm^{-2}, one additional cycle was performed at 1 mA cm^{-2} to check the capacity retention. The charge rate was constantly 1 mA cm^{-2} followed by a constant voltage step at 4.3 V to ensure complete delithiation of the cathode.

The EIS measurements were preceded by an open-circuit voltage (OCV) period of 20 h, and were carried out within a frequency range of 10 mHz and 300 kHz with 10 points per decade and applying a sinusoidal potential amplitude of 10 mV. All measurements were recorded on a VMP-3 electrochemical workstation (Biologic) and repeated at least three times to ensure results reproducibility.

Simulative Methods

In this section, we elaborate on the numerical methods employed; specifically shedding light on the generation of virtual electrodes by model-based insertion of the CBD, creation of domains with structural inhomogeneities, and the type of simulations conducted. A short description of the model and the corresponding parameters used is provided in Simulation framework and methodology section. Additionally, the constitutive equations are summarized in Table II. Nomenclature can be found in Table SI-1 of the Supporting Information.

Generation of virtual electrodes.—*Heterogeneous distribution of the CBD.*—Three-dimensional reconstructions of the electrodes obtained from synchrotron tomography serve as a basis for the generation of the virtual electrodes. As it is challenging to conduct a reliable reconstruction of the CBD phase from tomographic data, it is distributed on a model-basis using an in-house structure-generator at the contact points of AM particles.[31] The EDX-mapping of an electrode cross-cut is shown in Fig. 1a. The response in orange in the left section of the image is due to the flourine in the PVDF binder, signaling binder enrichment toward the surface of the electrode. This is validated by the congruent distribution of carbon conductive additive (in red) in the conjoining image.

As outlined previously, binder enrichment at the electrode surface can cause (i) a loss of preferred conduction pathways for electrons at the current collector and, (ii) formation of a dense layer of CBD at the electrode surface, inhibiting lithium-ion penetration into the electrode. In order to isolate and study the effects of these two phenomena, the tomographic was appended to create five virtual electrodes, each representing differing scenarios of CBD spatial distribution. This is graphically elucidated in Fig. 2.

The five different configurations shown in Fig. 2 have the corresponding physical prominence:

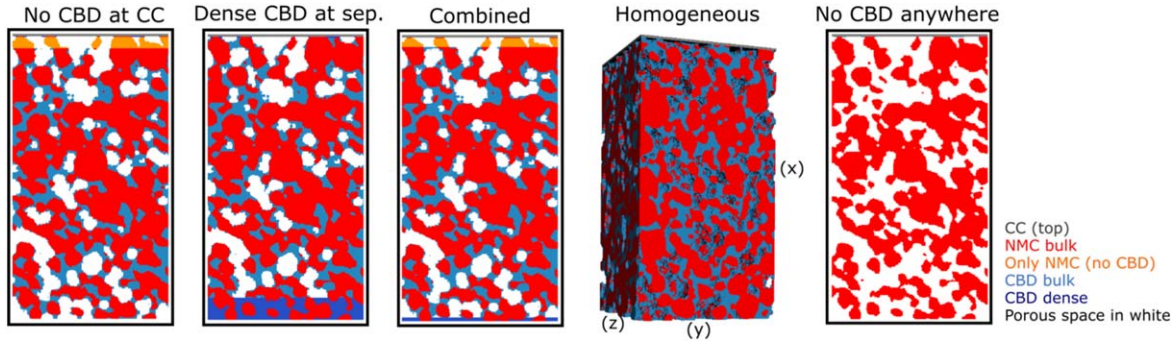

Figure 2. Illustrations of the different CBD configurations (2D slices are cross-sections in the through-direction to enable better visualisation. An example in 3D is shown for the "Homogeneous" case). The current collector (CC) is shown at the top, and the porous space is given in white. The identifier for each configuration is listed above the respective image. Through-direction of transport between anode and cathode is denoted by (x), whereas (y) and (z) are the in-plane coordinates. The dimensions of the electrodes are given in Table I.

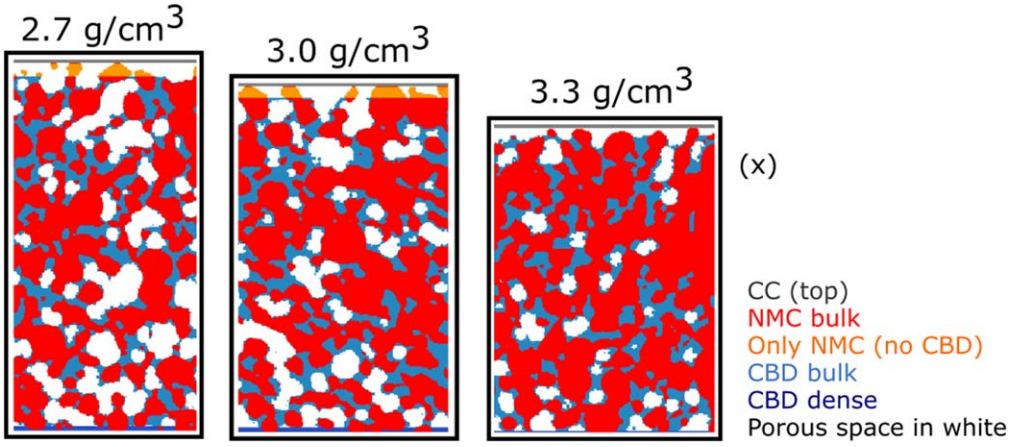

Figure 3. Phase distribution in representative 2D slices of the three different electrode densities for the "Combined" case extracted in the through-direction (x). Increasing the electrode density compresses the solid structure, reducing the heterogeneously distributed CBD layers. This becomes evident when one compares the image of electrode with density 3.3 gcm^{-3} with 2.7 g cm^{-3}.

(i) "No CBD at CC": we describe the loss of electronic conduction pathways by assuming an extreme case, where a solid layer adjacent to the current collector is devoid of CBD (refer to the region in orange in Fig. 2). The local effective electronic conductivity in this layer is given by that of NMC622.
(ii) "Dense CBD at sep.": binder enrichment at the electrode surface results in a dense layer of accummulated CBD beside the separator (given in dark blue).
(iii) "Combined" is a combination of both the phenomena i) and ii); i.e. CBD-absent layers adjacent to the CC (in orange) and CBD-dense layers adjacent to the separator (in dark blue).
(iv) In "Homogeneous", the CBD is distributed uniformly across the electrode thickness.
(v) Additionally, a fifth control configuration, "No CBD anywhere", is studied, where the entire domain is devoid of any CBD material.

The thickness of the different layers in configurations (i) through (iii) is adjusted iteratively to reproduce the the real part of the impedance measurements on symmetrical cells, i.e. the width between the two minima of the imaginary impedance response (see Fig. 6). It is to be noted, that the total volume fraction of the CBD was not kept constant between the several configurations (refer to Table SI-3 in the Supporting Information). Therefore, we can expect a qualitative prediction of the electrochemical performance measurements. Still, these observations can give important insights on limiting processes owing to heterogeneities in the electrode microstructure.

Variation of electrode density.—The configurations representing the scenarios described in Heterogeneous distribution of the CBD section are created for all electrode densities (2.7, 3.0 and 3.3 g cm^{-3}). As calendering alters the thicknesses of the CBD-absent/rich layers, these were iteratively adjusted to match the impedance experiments. Figure 3 shows the 2D cross-sections of the ``Combined" case for the three electrode densities. Refer to Table I and Table SI-3 in the Supporting Information for sizes of the geometries.

Simulation framework and methodology.—All simulations presented in this article are performed with the development branch of the **B**attery and **E**lectrochemistry **S**imulation **T**ool (BEST).[55] The simulations are able to provide the temporal and spatial distribution of lithium/ion concentration, potential, and temperature. Constitutive equations are summarized in Table II and a detailed derivation is given in Refs. 31, 50, 51. To assist in the investigation of the influence of CBD distribution on the cell performance, we run symmetric cell EIS and HC galvanostatic delithiation simulations. The cell setup for these two methods are shown in the next sections.

Electrode cutouts.—In order to account for the variations within the microstructure of the electrodes arising from the processing steps, three non-overlapping cutouts with the same dimensions in the in-plane direction and the complete thickness in the through-plane direction are assessed. This approach additionally provides statistical

Table I. Thickness of layers with varying CBD content at all electrode densities. Configuration (i) is "No CBD at CC", (ii) is "Dense CBD at sep.", (iii) is "Combined", and "Hom." stands for "Homogeneous" case. The cross-section of the tomographic data is given by a quadrilateral with identical length (y) and width. Thickness is given by x. The colours in brackets correspond to the regions in Fig. 2.

Configuration	Hom.	(i)	(ii)	(iii)
2.7 g cm^{-3}		y = 74 μm ; x = 152.9 μm		
CBD absent (orange)	0	5.7	0	5.3
Bulk (blue)	152.9	147.2	138.9	141.8
CBD dense (dark blue)	0	0	14.0	2.2
3.0 g cm^{-3}		y = 79 μm ; x = 141.9 μm		
CBD absent (orange)	0	5.3	0	4.4
Bulk (blue)	141.9	136.6	130.6	134.9
CBD dense (dark blue)	0	0	11	2.6
3.3 g cm^{-3}		y = 83 μm ; x = 116.9 μm		
CBD absent (orange)	0	0.4	0	0.4
Bulk (blue)	116.9	116.5	111.6	116.1
CBD dense (dark blue)	0	0	5.3	0.4

information on structural fluctuations on the length scale of a few micrometers.

Virtual cells.—The virtual cells either consist of a separator and two identical NMC622 electrodes or an NMC622 electrode with a lithium-metal anode corresponding to the symmetrical cell and HC setup, respectively (Fig. 4). Each electrode is in contact with the current collector. The cathodes were embedded with up to six voxels in the current collector to ensure good contact and numerical convergence. A summary of the parameters and properties used for each of these simulations is provided in Table SI-1 of the Supporting Information.

Separator.—The separator is modelled as a porous membrane of 10 μm thickness, comprising of 50% electrochemically inactive material. The bulk electrolyte is assumed to occupy the pore spaces homogeneously.

Bulk electrolyte.—In the electrolyte, the concentration and electrochemical potential of lithium ions is solved for by the conservation equations for mass and charge, given by Eqs. 1 and 2 in Table II, respectively. The bulk electrolyte transport parameters used for $LiPF_6$ in EC/EMC at 298 K (ionic conductivity, transference number, diffusion coefficient, thermodynamic factor) are as measured by Nyman et al.[56]

Lithium anode.—The lithium anode is modelled as a 1.31 μm long flat electrode with an infinite source of lithium available for intercalation at the cathode. The kinetics constants are calibrated against literature data[57] reported in previous work.[1]

Cathode active material.—At the interface of the active material and electrolyte, we describe the intercalation reaction of lithium-ions by a Butler-Volmer type Eq. 13 and additionally consider contributions of the electric double-layer 14 in parallel to the Faradaic current. The double-layer has a constant areal capacity and is modelled as a parallel plate capacitor. The coupling conditions at the interface between the active material and the electrolyte are given by Eqs. 9–12. The concentration of lithium (c_{So}) in the active material can be calculated by solving the corresponding conservation equation of mass given by Eq. 3. Finally, an additional equation for the calculation of the electric potential in the solid phase is required. At the AM and CBD solid subdomain interface, the model allows for a continuous flow of electrons, thereby accounting for the influence of the CBD distribution on the electronic conductivity of the AM particles. The conservation of charge is given by Eq. 4 and the flux

Table II. The constitutive equations of the Li-ion battery model used in this work. Details of the derivation can be found in Refs. 50, 51 ε in Eq. 16 is 50%. For nomenclature, refer to the Supporting Information Table SI-1. Abbreviation "Elyte" stands for Electrolyte.

Phase	Material balance	Charge balance
Elyte	$\frac{\partial c_{El}}{\partial t} = -\vec{\nabla}\cdot\vec{N}_{El}$ (1)	$0 = -\vec{\nabla}\cdot\vec{j}_{El}$ (2)
AM	$\frac{\partial c_{So}}{\partial t} = -\vec{\nabla}\cdot\vec{N}_{So}$ (3)	$0 = -\vec{\nabla}\cdot\vec{j}_{So}$ (4)
Phase	**Lithium flux**	**Charge flux**
Elyte	$\vec{N}_{El} = -D_{El}\vec{\nabla}c_{El} + \frac{t_+}{F}\vec{j}_{El}$ (5)	$\vec{j}_{El} = -\kappa_{El}\vec{\nabla}\varphi_{El} + \kappa_{El}\frac{1-t_+}{F}\left(\frac{\partial \mu_{El}}{\partial c_{El}}\right)\vec{\nabla}c_{El}$ (6)
AM	$\vec{N}_{So} = -D_{So}\vec{\nabla}c_{So}$ (7)	$\vec{j}_{So} = -\sigma_{So}\vec{\nabla}\Phi_{So}$ (8)
Interface	**Lithium flux**	**Charge flux**
Elyte	$\vec{N}_{El} = N_{El}\cdot\vec{n}_A = \frac{i_{BV}+i_{DL}}{F}$ (9)	$\vec{J}_{El} = J_{El}\cdot\vec{n}_A = i_{BV} + i_{DL}$ (10)
AM	$\vec{N}_{So} = N_{So}\cdot\vec{n}_A = \frac{i_{BV}}{F}$ (11)	$\vec{J}_{So} = J_{So}\cdot\vec{n}_A = i_{BV} + i_{DL}$ (12)
	Faraday current: $i_{BV} = i_0\left[\exp\left(\frac{\alpha F}{RT}\eta\right) - \exp\left(\frac{(1-\alpha)F}{RT}\eta\right)\right]$ (13)	
	Double layer current: $i_{DL} = -C_{DL}\cdot\frac{d}{dt}(\Phi_{So} - \varphi_{El})$ (14)	
Elyte—AM	$i_0 = i_{00}\, c_{El}^{\alpha}\, c_{So}^{(1-\alpha)};\quad \eta = \Phi_{So} - \varphi_{El} - U_0(c_{So})$ (15)	
Elyte in CBD—AM	$i_{eff} = \varepsilon\, i_0;\quad \eta = \Phi_{So} - \varphi_{El} - U_0(c_{So})$ (16)	
Elyte—Li	$i_0 = i_{00}\, c_{El}^{\alpha};\quad \eta = \Phi_{So} - \varphi_{El}$ (17)	

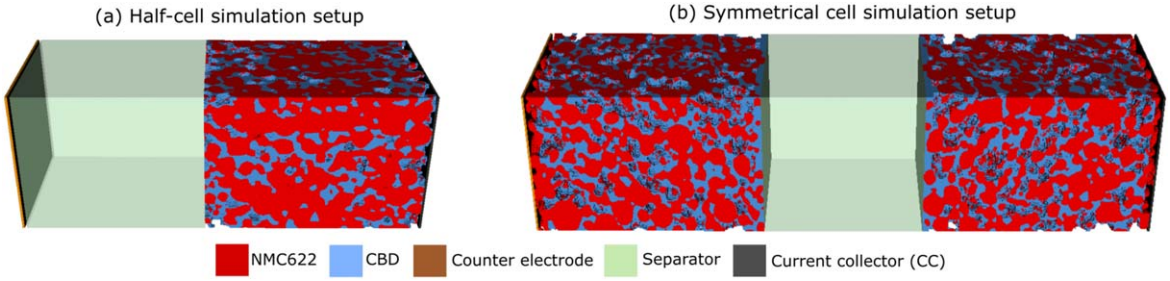

Figure 4. Simulation setups for a (a) HC galvanostatic lithiation of the cathode and (b) electrochemical impedance spectroscopy in symmetric cell configuration. The pore space is transparent.

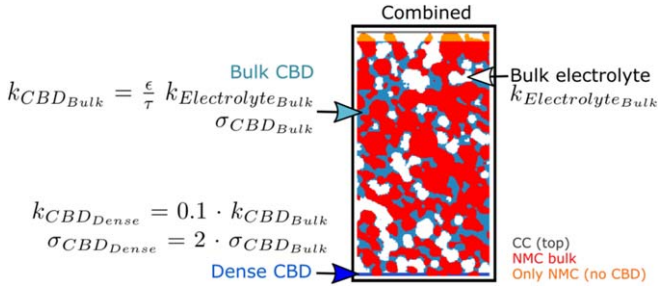

Figure 5. Effect of heterogeneous CBD distribution on the effective transport parameters in different phases illustrated for a "Combined" configuration.

of electrons is calculated as per Eq. 8. The fit data for the chemical diffusion coefficient (D_{So}) and electronic conductivity (σ_{So}) as a function of the c_{So} is given in Ref. 58.

CBD.—As previously mentioned, the CBD is distributed on a model-basis at the contact points of AM particles, and is assumed to have an isotropic porosity of 50%, that allows ion conduction. The effective ion transport is given by the effective tortuosity values as determined in [45] for a two-layer electrode with a total CBD volume fraction of 11.54 vol-%, compared to 11.2-vol-% (before calendering) used in this study. The two-layered electrodes showcased a more gradual binder distribution gradient, as the two layers were inherently manufactured with different suspensions. Hence, the effective tortuosity factor for a two-layer electrode, where the CBD is placed based on a morphological closing of the active material that takes the EDX information into account, was chosen.

This factor was applied in this study as a function of the CBD distribution. In the bulk of the electrode, $\kappa_{CBD_{Bulk}} = 0.12 \cdot \kappa_{Electrolyte_{Bulk}}$,[45] where κ is used to describe ionic conductivity. At the separator, due to the enrichment of the polymeric binder and its role in impeding ion transport, this factor is set to be higher (see Fig. 5), i.e. $\kappa_{CBD_{Dense}} = 0.1 \cdot \kappa_{CBD_{Bulk}}$. Once the effective transport properties are defined, the conservation equations for electrolyte transport (Eqs. 1 and 2) are solved to determine the lithium ion concentration within the CBD pore network. At contact points between the AM and CBD, the specific active electrolyte surface area is reduced to 50% (proportional to CBD porosity), downscaling the AM-Electrolyte intercalation and double-layer kinetics at these points by the same factor (see Eq. 16). Note, that there are no chemical reactions modelled at the interface of the solid fraction of the CBD and the liquid electrolyte.

Finally, the electric transport in the CBD solid subdomain is determined by the conservation Eqs. 4 and 8. Figure 1 shows that there is also an aggregation of the conductive additive at the electrode surface ($\sigma_{CBD_{Dense}}$), thereby increasing the electronic conductivity in these layers. Hence, $\sigma_{CBD_{Dense}} = 2 \cdot \sigma_{CBD_{Bulk}}$. At the CBD and AM solid interfaces, the model allows for a continuous flow of electrons.

Electrochemical simulations.—All electrochemical simulations, including effective conductivity, are run on the same set of virtual electrodes, in order to deconvolute the effect of binder distribution on the electrode performance. A detailed description of the methodology for the calculation of impedance spectra can be found in our previous publications.[31,59]

Effective conductivities.—The effective conductivities of each of the configurations for all electrode densities are solved for numerically. The steady-state Poisson equation (Eq. 1) is solved with a constant current density boundary condition (as elucidated in Ref. 43). The potential distribution then takes into account the differing effective conductivities of the various materials in the electrode. Note, that the calculations are performed separately for the solid (solid CBD fraction + cathode AM) and liquid phase (porous CBD fraction + bulk electrolyte). Refer to Simulation framework and methodology section of the Supporting Information sheet for the effective electronic and ionic conductivities of the electrodes at differing electrode densities and CBD distributions.

$$\sigma_{effective} = j\frac{\Delta x}{\Delta \phi}. \quad [1]$$

Electrochemical Impedance Spectroscopy (EIS).—The impedance spectra are calculated by the potential-step and current relaxation technique[60] for symmetric cells under steady-state. A detailed description is provided in our previous publication.[31] Starting in a steady-state, we excite the cell with a small potential step of 2 mV, and monitor the resulting current signal. Finally, the impedance at different frequencies is evaluated by dividing the Fourier transform[61] of the voltage with the current signal. Furthermore, symmetric cells (in comparison to HCs) provide the advantage that one can isolate the response due to a single electrode chemistry, without it being mangled by a counter electrode. The results of these simulations are presented in Symmetric cell impedance spectra section.

In the experiments, the cells are subjected to blocking electrolyte conditions, resulting in an ideally polarisable electrode where a current is only induced by capacitive effects. Blocking conditions in the simulations are achieved by setting the cathode AM potential close to complete lithiation, resulting in low ion intercalation at the AM and electrolyte interface and, correspondingly, low AM electronic conductivity.

Galvanostatic discharge.—Half-cell (HC) galvanostatic delithiation (of the anode) simulations are run with lithium metal as the counter-electrode. The initial lithiation degree of the electrodes is set to correspond to a cell voltage of 4.3V, following the experimental conditions. In all simulations, we start with a homogeneous initial concentration of lithium in the active material, and lithium ion in the electrolyte. All virtual electrodes of different electrode densities were discharged with current densities of 1.5, 3.0, 6.0 and

12 mA cm^{-2} down to a lower cutoff voltage of 3.0 V. Results of the HC simulations are presented in Galvanostatic delithiation section.

Results and Discussion

The results of the electrochemical methods discussed above are presented in this section. The connection between microstructural heterogeneities and the cell performance can be established via symmetric cell EIS. More specifically, we use the EIS data to qualitatively inform the different scenarios of CBD distribution by comparing experiment and simulation. In a next step, we simulate HC discharge phenomena on the same 3D microstructure-resolved geometries. Hence, this Section is divided into two parts: first, we dive into the results of the impedance spectra simulations and finally, we corroborate this data with HC delithiation simulations at different discharge currents. The initial conditions and material parameters applied are identical for all impedance simulations. Hence, the reason for the differences in responses is exclusively due to structural variations in the CBD distribution.

Symmetric cell impedance spectra.—In this section, we will analyze the impedance responses of (i) different CBD structural scenarios firstly for the 3.0 g cm^{-3} density electrode and then (ii) under varying electrode densities, and compare them to experimental data. There were two EIS measurements per electrode, marked in gray as Exp. Data 1 and 2 in Fig. 6. For the sake of clarity, unless otherwise mentioned, all the results shown in the upcoming Sections are restricted to one representative electrode cutout only. The data regarding all three cutouts of the segmented tomographic image data is provided in Section SI 4.2.1. of the Supporting Information. We start with a short analysis of the experimental measurements before introducing the simulated data.

Effect of structural scenarios.—Experimental data.—Figure 6 shows the results for impedance measurements of a symmetrical cell under blocking conditions for a 3.0 g cm^{-3} density electrode. Under ideal conditions (uniform electronic and ionic conductivities across the electrode), we expect a linear increase of the imaginary part in a 45 degree angle to the real axis.[31,32] However, in our measurements, we observe two characteristic regions: a high frequency region (>2000 Hz), and a region with linear increase region of the imaginary part. The indicated frequency ranges are not consistent with the typical values reported for charge-transfer kinetics at the interface of AM and electrolyte. In the next section, we show how this phenomenon can be reproduced due to structural heterogeneities in the electrode.

Simulation results.—Figure 7 shows the impedance spectra of symmetric cells from the simulations (in solid lines) alongside the experimental data (marked by symbols). Reference configurations with a homogeneous CBD distribution or the "No CBD anywhere" case show expected trends, namely a linear increase of the imaginary part in the first region of the spectra. However, in the "Homogeneous" case, the width of the real part of the impedance is smaller compared to the experimental data, and the scenario without any CBD has an order of magnitude higher impedance. This emphasises the relevance of the electronic network.

As elucidated before, the thicknesses of the respective heterogeneous layers in the various scenarios were adjusted so as to closely match the real part of the experimental impedance (i.e. the width of the semi-circle from the first intercept where the imaginary part is zero, to the second minima of the imaginary impedance). Since the semi-circle occurs at such large frequencies, it highlights the faster processes occurring in the electrode, such as the electron transport within the solid matrix controlled by the inherent conductivities and connectivities of the solid CBD and cathode AM, and ion transport within the pore space. Hence, both the absence or dense accumulation of the CBD promotes regions of high potential gradients in the solid and electrolyte phase. The high frequency semi-circle is,

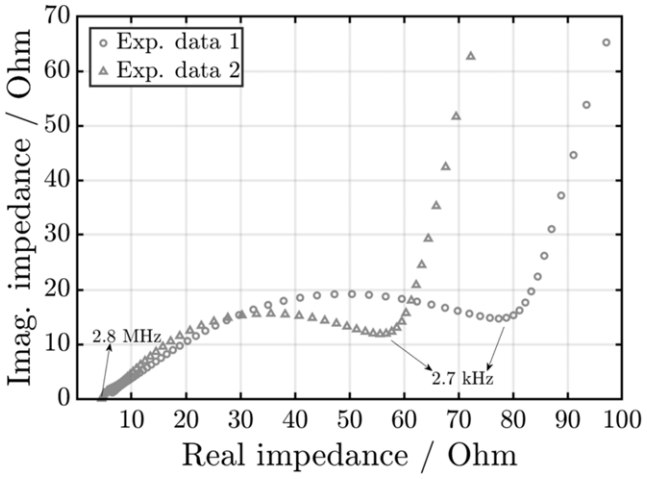

Figure 6. Nyquist plot of EIS measurements conducted under blocking conditions in a symmetrical cell setup. The figure shows the high-frequency data of measurements on two electrode samples with density 3.0 g cm^{-3}. The abbreviation "Exp." stands for experimental data.

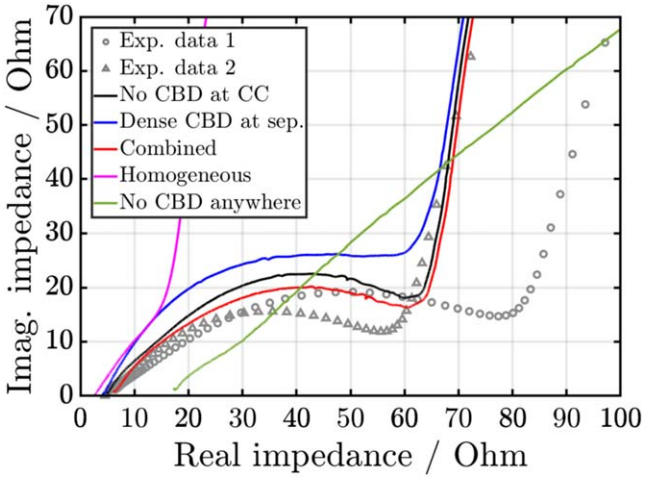

Figure 7. Nyquist plot of EIS measurement and simulation data of electrodes with density of 3.0 g cm^{-3} in a symmetric cell configuration. Simulations performed on the same 3D reconstruction with different CBD distribution are represented by solid lines. Simulation labels correspond to the configurations illustrated in Fig. 2. Both the simulation (in solid lines) and experiments (in gray markers) were conducted under blocking conditions. The abbreviation "Exp." stands for experimental data.

therefore, only prominent in configurations that have some heterogeneity in the CBD distribution, indicating such microstructural non-uniformities to be present in the real electrodes studied here.

A distribution of these potentials across the electrodes leads to varying degrees of dominance of either the ionic or electronic current with respect to time. Looking at the individual cases more specifically, the "Dense CBD at sep." has binder enrichment at the electrode surface, and hence, presents a constriction to ion transport. As the number of accumulated CBD layers at the separator required to mimick the impedance data is much larger than the number with poor electronic connection to the CC (seen from Table I), the "Dense CBD at sep." case has a higher total impedance at shown frequencies when compared to the "No CBD at CC" case. Combining both the effect of absent CBD at the CC in "No CBD at CC", and the enriched layers in "Dense CBD at sep.", gives the "Combined" scenario which best agrees with the experimental data. This configuration is also able to mimic the flatter semi-circle as seen in the experiments. This is an indication that the "Combined" case is

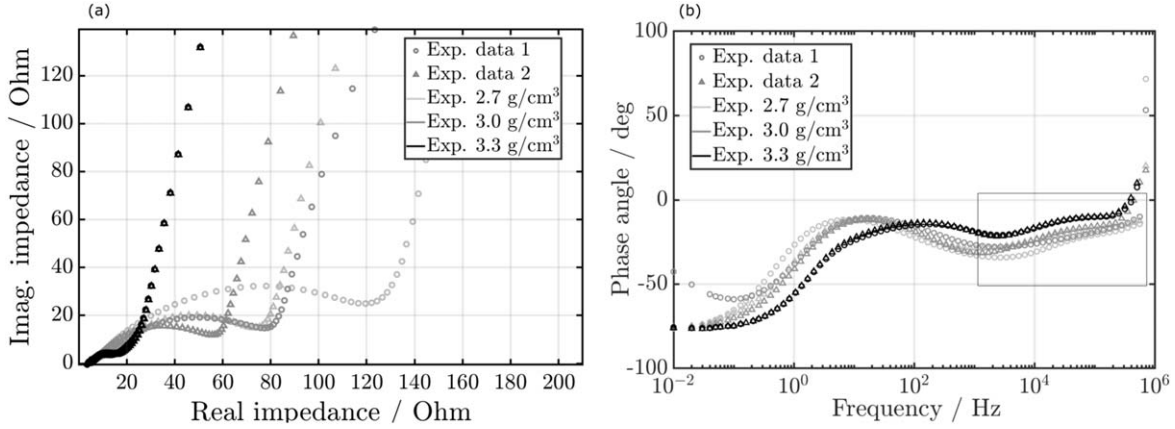

Figure 8. Impedance measurements on electrodes in a symmetric cell configuration. Different shades of gray indicate variations in electrode density between 2.7 and 3.3 g cm^{-3}. For each density we performed two measurements. (a) Nyquist plot of impedance spectra showing the high-frequency semi-circle. (b) Corresponding phase angle plots for the experimental data on electrodes with densities 2.7, 3.0 and 3.3 g cm^{-3}. The experiments were conducted under blocking conditions. The abbreviation "Exp." stands for experimental data.

most representative of electrodes studied in this work, however overall, the impedance spectra of the heterogeneous electrodes qualitatively match the experimental data. The imaginary part of the spectra is slightly more prominent in the simulations, owing to the qualitative nature of the study. For further insight into the corresponding effective transport parameters of the studied structures, refer to Section SI 3.2. of the Supporting Information.

In order to ensure that the high-frequency semi-circle behavior was not an artefact of the kinetics and bulk CBD transport properties employed in the model, further parallel studies were conducted with varying kinetic constants and bulk CBD transport coefficients. There were no variations in this behavior when the intercalation constant or double-layer capacitances were changed by a factor of 10% in either direction (see Section SI 4.1. in the Supporting Information). Moreover, the chosen bulk CBD transport parameters did not alter the 45 degree angle response of the "Homogeneous" case. Hence, we can deduce that the high-frequency semi-circle is indeed a product of structural heterogeneities due to the CBD distribution.

In summary, microstructural defects within the electrode matrix causes an inhomogeneous polarization of the electrode, leading to an additional semi-circle in the impedance spectra at frequencies higher than the characteristic frequencies typical of charge transfer kinetics. We could demonstrate that the experimentally prepared electrodes have both electronically limiting (low amount of conductive carbon at the CC), and ionically limiting (dense binder phase at the separator) heterogeneities, where the former is more dominating. The "Homogeneous" scenario shows the lowest impedance, hence it is expected to perform best at all HC discharge currents, while the "Combined" scenario is expected to be in line with the experimental data. Therefore, we will restrict ourselves to the latter configuration when comparing the effect of electrode calendering on the impedances in the next section.

Effect of calendering.—Experimental data.—Figure 8(a) shows the symmetric cell impedance measurements under blocking conditions on electrodes with densities of 2.7, 3.0 and 3.3 g cm^{-3}. The darker the gray shade, the higher the electrode density. With increasing calendering rate or electrode density, the width of the high-frequency semi-circle decreases. Calendering of the electrodes enhances the electronic contact between the conducting solid particles themselves and the CC, while reducing the porosity and increasing the pore transport resistance. This process not only compresses the bulk electrode, but also the layers with heterogeneities in the CBD fraction, thereby decreasing the impedance registered by the high-frequency semi-circle with an increase in calendering density. This decrease of the impedance indicates that

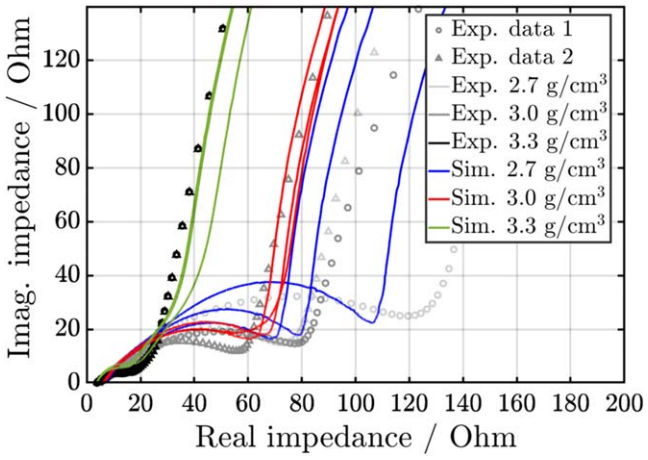

Figure 9. Nyquist plot of EIS data from simulation (solid lines) and experiment (symbols) under blocking conditions. Different colors indicate simulations on 3D reconstructions for the "Combined" scenario with different electrode density. For each density we performed three simulations on three cutouts highlighting the heterogeneity detected in image data. Corresponding measurement data is included as open symbols in the graph and also shown in Fig. 8. The abbreviations "Exp." and "Sim." stand for experimental data and simulation results, respectively.

both a CBD deficient layer and a CBD rich layer are present, however the former dominates the electrode impedance. Impedance spectra at higher electrode densities are close to the ideal behavior of the homogeneous electrode, and show a lower standard deviation between the cutouts. This is also paralleled by the simulations.

Simulation results.—Figure 9 shows the impedance response for the three electrode densities under the "Combined" scenario along with the corresponding experimental data. Simulation results of the other scenarios are reported in the Supporting Information (see Section SI 4.2.1.). The three lines for each electrode density represent the three cutouts from different regions of the electrode. In all cases, the thicknesses of the heterogeneous layers was adjusted to reproduce the experimental data, while retaining the same total electrode thickness. Refer to Table I for data on the average dimensions.

Consistent with the experimental data, the higher density electrodes exhibit a smaller impedance in the high-frequency region. As seen in Table I, the number of enriched and absent CBD layers

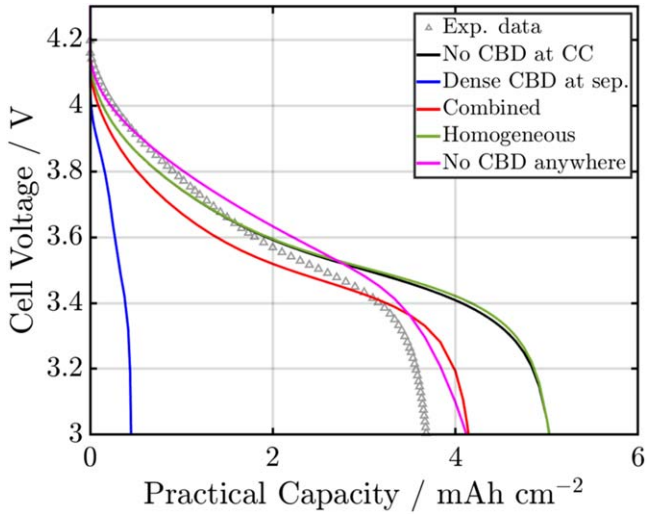

Figure 10. Results of HC discharge simulations on electrodes with density 3.0 g cm^{-3}. Discharge is simulated between 4.2 and 3.0 V with constant discharge current density of 6 mA cm^{-2}. Solid lines with different colors represent simulation data of different CBD configurations introduced in Fig. 2. Measurements at the same discharge current are given by gray triangles.

are thinner at higher electrode densities. This leads to fewer regions of large potential jumps in the electrode, and hence, a lower electrode polarization. Also, simulations on electrodes with low electrode density consistently reproduce the experimental data, including the aspect of higher standard deviation between the three cutouts.

In the next section, we attempt to corroborate the impedance results summarised in the previous sections with the HC discharge data.

Galvanostatic delithiation.—The galvanostatic discharge simulations were conducted at 4 different discharge currents: 1.5, 3.0, 6.0 (approximately 1C), and 12 mA cm^{-2}. This was done for the various structural scenarios, electrode densities and cutouts of the tomographic image data. For clarity, unless otherwise specified, all the results presented here are for one cutout only. For insight into all the data, we direct the interested reader to the Supporting Information (see Section 4.2.2.). The discharge curves are simulated in the voltage window between 4.3V and 3.0V. The results for the mid-density electrode at 1C will be discussed first, before addressing the effect of changing C-rates. Finally, we will discuss the influence of calendering on delivered electrode capacities.

Effect of structural scenarios at 1C.—The discharge curves at 6 mA cm^{-2} for the electrode with 3.0 g cm^{-3} density are shown in Fig. 10. The curve marked gray represents the experimental data, while those in solid colours are simulated results.

As expected, the areal capacity of the "Homogeneous" electrode is the highest, retaining about 80% of its capacity from 1.5 mA cm^{-2}. At this current density, the benefit of both highly conductive electronic networks and ionic pathways is evident. The "Homogeneous" scenario can also be regarded as the benchmark for the other scenarios.

The "No CBD at CC" scenario performs almost on par with the "Homogeneous" case, even though the impedance in the symmetrical cell setup was significantly larger for the former. Except for the CBD-absent layer, the backbone electrode microstructure is identical to the "Homogeneous" scenario (due to this similarity, the subsequent distributions for the "Homogeneous" case are not redundantly shown). This indicates that small layers of poor electronic contact to the CC do not significantly affect discharge capacities. Interestingly, the scenario "No CBD anywhere", shows remarkable electrochemical performance despite very poor effective electronic conductivity. Furthermore, this scenario agrees best with the experimental data. However, this is clearly not the most probable scenario either in our study, or practically. This demonstrates that ionic transport is the decisive process determining the capacity of the cell, atleast at this current density. The scenario with a dense CBD at the separator represents the extreme case of lithium-ion transport limitations. In this case, we observe a significant loss in capacity, underlining the impact of inhomogeneous CBD distribution on lithium-ion transport and performance. Although in qualitative agreement with impedance data, the two extreme scenarios "No CBD at CC" and "Dense CBD at sep." either over- or underestimate the discharge capacity. Hence, we conclude that the combination of the two indeed provides the most realistic scenario to reproduce both the impedance and lithiation experiments. This can be better visualised in Fig. 11.

Figure 11 shows the state-of-charge (SoC) distribition within the cathode AM for four chosen configurations. In the "No CBD anywhere" scenario, the overpotential for intercalation at the CC is lowest, due to poor electronic connection to the bulk electrode, resulting in a low AM SoC in this region. On the contrary, the "Dense CBD at sep." scenario showcases a higher AM SoC at the separator. The ion transport is restricted to the few larger pores connected to the separator, as there is an impediment to transport into the bulk electrode pore space due to the binder enrichment. This is also prominent in the "Combined" case. The lithium-ion flux across the separator for the "Combined" case is higher than for the "Dense CBD at sep." case due to the thinner accumulated binder. This is well-visualised in Fig. 12, which shows the lithium-ion flux across the electrode. It is clear, that the lithium-ion transport preferentially occurs in the mesoporous space due to the high ion transport tortuosity in the porous CBD. The obvious advantage of accessible porous volume for ion transport into the electrode is demonstrated by the "No CBD anywhere" scenario, reflected in its relatively high discharge capacity.

We shall now look into how changing the discharge current density affects the transport in these various scenarios.

Effect of discharge current density.—Figure 13 shows the discharge areal capacity of the different configurations at increasing current densities for the electrode with a density of 3.0 g cm^{-3}. In this graph, we present the average discharge capacities of all three electrode cutouts, normalised to their nominal capacity value (done the same way for the experimental data points). The triangular marker in gray represents the experimental data. The nominal capacity values for all the electrodes and their cutouts can be found in the Supporting Information (see Table SI-4).

All scenarios show the expected drop in capacity with increasing discharge current. The scenario with a homogeneous CBD distribution, serving as a benchmark in our study, provides the highest capacity up to currents of 6 mA cm^{-2}. Interestingly, the hypothetical scenario without any CBD anywhere shows the highest capacity at the highest current, in-turn also significantly overestimating the capacity compared to experiments. This sheds light on the limiting effect of ion transport on battery performance, especially at higher discharge currents.

The "No CBD at CC" scenario performs on par with the "Homogeneous" case at all current densities, showing only smaller capacities at low current densities due to its poor electronic conduction at the CC. In contrast, the scenario with a dense CBD accumulation at the separator causes a rapid loss of capacity with increasing current. Thereby significantly over-predicting the

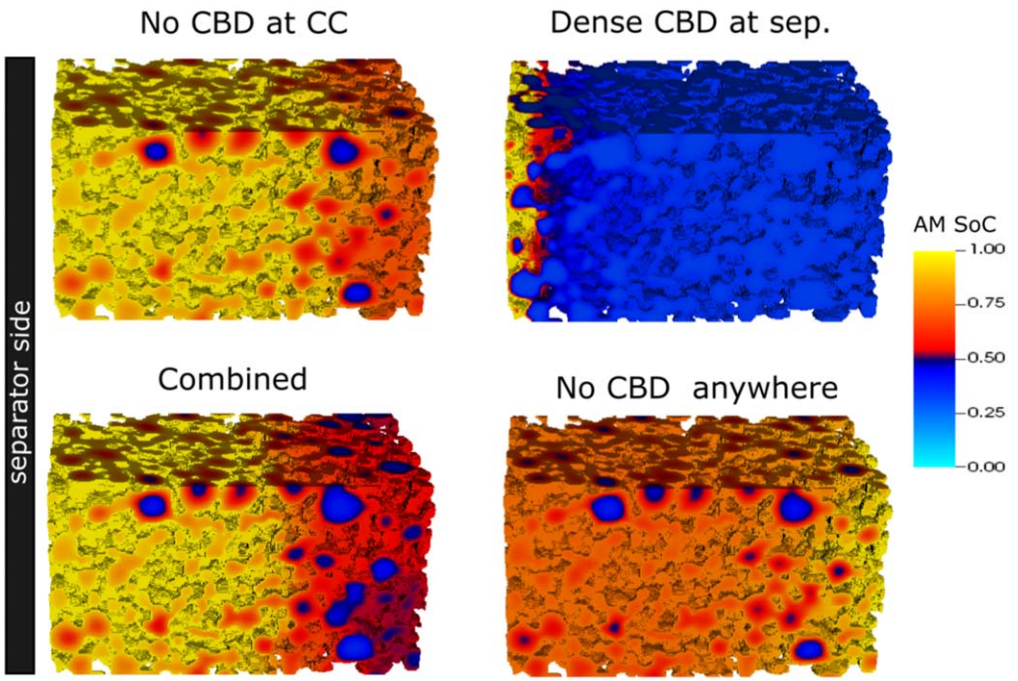

Figure 11. 3D distribution of the cathode AM state-of-charge (SoC) representing the normalized lithium distribution in an electrode with a density of 3.0 g cm^{-3} at the lower cutoff (3.0 V) of a lithiation simulation with 6 mA cm^{-2} constant current. Different panels represent the scenarios introduced in Fig. 2. The separator is on the left hand side of the 3D distribution in each panel and the current collector is to the right.

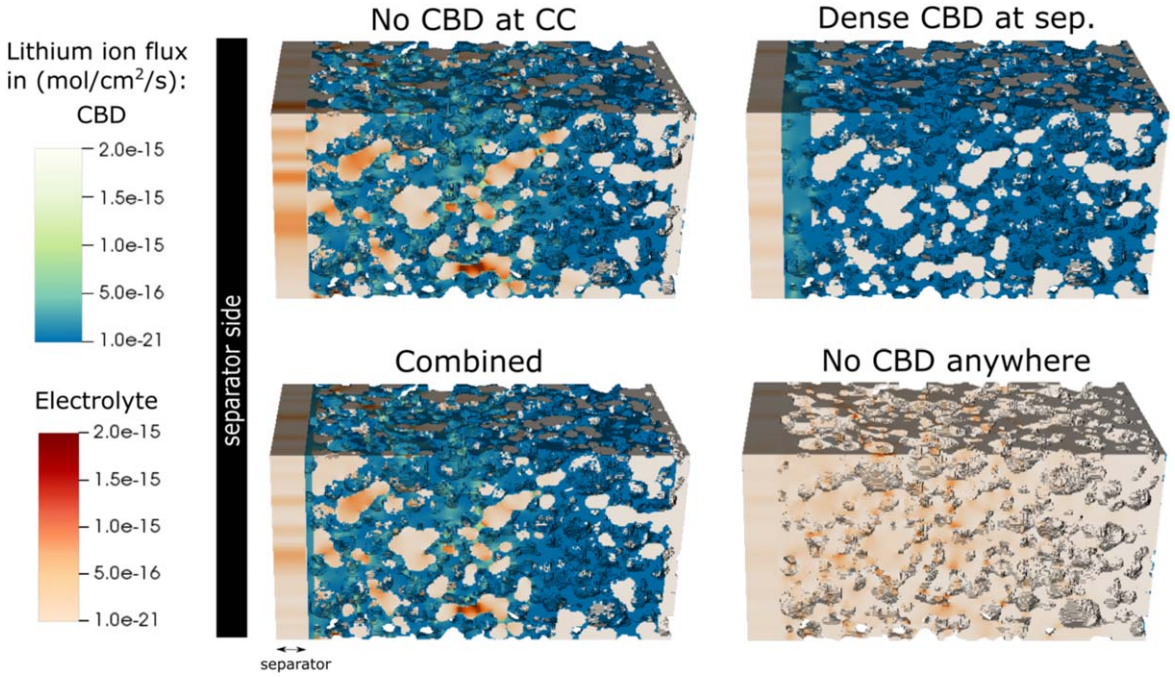

Figure 12. Flux of lithium ions within the pore space of an electrode with a density of 3.0 g cm^{-3}. Different panels represent the scenarios introduced in Fig. 2. The separator is on the left hand side of the 3D distribution in each panel and the current collector is to the right. The color scales indicates the flux of lithium ions in the electrolyte within the mesopores (orange color scale) and CBD (blue color scale) at the lower cutoff voltage 3.0V after lithiation with a constant current of 6 mA/cm^2. The active material is transparent.

influence of transport limited ions in the electrolyte. As previously surmised, the "Combined" scenario demonstrates the best agreement with the experimental data.

This further corroborates our understanding that the electrodes investigated in this work have both electronically and ionically non-uniform networks and that this distribution critically affects the electrode performance. The effect of different scenarios on concentration and flux distributions at different currents is presented in the Supporting Information, providing additional insights on limiting processes (see Section SI 4.2.2.).

Effect of calendering.—In this section we will address the effect of electrode calendering, with a specific focus on the "Combined" case at all discharge current densities. Figure 14 shows the experimental and

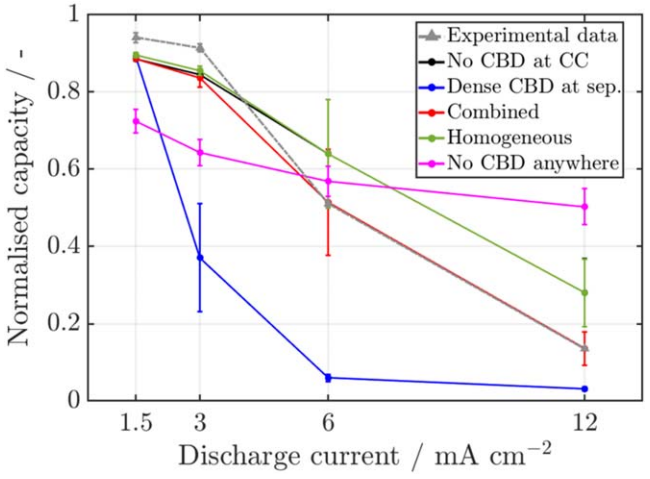

Figure 13. Summary of the discharge capacity for all scenarios introduced in Fig. 2. Discharge capacity was determined at the lower cutoff voltage of 3.0 V after constant current discharge from 4.2 V. Capacities for both the experiments (gray color) and simulations (solid lines) were normalised to their theoretical capacity. The figure focuses on an electrode with density of 3.0 g cm^{-3}.

simulation results at increasing discharge currents. The simulation results are given in color and the experimental data in gray-scale.

Experimental results.—We can see from Fig. 14a that the lowest density electrode, 2.7 g cm^{-3}, provides the highest practical capacity at all currents. This electrode has a 60% higher ionic conductivity than the 3.3 g cm^{-3} electrode and hence, a much lower pore transport impedance (see Supporting Information Section SI 3.2.). Electrodes with 3.0 and 3.3 g cm^{-3} densities show similar performance in the rate tests. However, the highest density electrode provides a slightly lower capacity at all currents. This trend is in-line with our previous conclusion on the different scenarios: slow ionic transport, in this case due to lower porosity, has a significantly more effect on performance compared to reduced effective electronic conductivity.

Simulation data.—Figure 14b shows the corresponding simulation results. Symbols indicate the average of the three electrode cutouts and the plot additionally shows the standard deviation at each data point. Generally, simulations are in-line with the experimental data (in gray). The electrodes all match the trend seen in the experiments except at the lowest current density. At 1.5 mA cm^{-2}, eventhough the individual capacities of the electrodes are comparable to the experiments, the shift between the electrode densities is not as obvious as in the experimental data. With increasing current densities, the resulting capacities diverge and match the trend as seen in the measurements.

Looking at each electrode density individually, we observe good agreement between the experiments and simulations for the electrodes with a density of 2.7 g cm^{-3}. Interestingly, the standard deviations are smaller here, in comparison to the wider spread seen in the corresponding impedance data. Deviations in the impedance spectra can be allocated to electrical properties, which is less pronounced in the discharge simulations.

When considering the mid-density electrode, again, a good agreement to the experimental data is seen. However, we also observe larger deviations in practical capacities, which is arising from differences in the ionic conduction pathways between the three cutouts. We have to emphasize, that in our study, we only adjust the thicknesses of the layers to the impedance data. Hence, the information is limited and does not allow to deduce the real configuration in the electrodes. Still, the qualitative agreement with the experimental data indicates that we assign observed features in the impedance spectra to the relevant transport processes.

In order to visualise these processes, Fig. 15 illustrates the distribution of the lithium-ion flux and cathode AM lithiation grade across the electrode for all the densities at 6 mA cm^{-2} discharge current. The flux of the lithium ions in the electrolyte indicates the active volume of the electrode. With increasing electrode density, the region with high flux densities close to the separator decreases. At a density of 2.7 g cm^{-3}, around two-thirds of the electrode shows high ionic flux density and a high lithiation of the cathode AM in the corresponding concentration distribution. Despite the high contact resistance, due to the low electronic conductivity close to the CC, there is moderate intercalation in this region. This confirms that thin layers without sufficient CBD network have a moderate effect on the capacity, yet a significant effect on the symmetric impedance. At increasing current densities (see Supporting Information Section 4.2.2.), only one-third of the 2.7 g cm^{-3} electrode shows high flux of lithium ions. As a consequence, the utilization of the cathode AM is significantly lower. Although the capacity drop at this current in the 3.3 g cm^{-3} electrode is most drastic, visually, the length of lithiated AM as a fraction of the total electrode thickness is higher here than

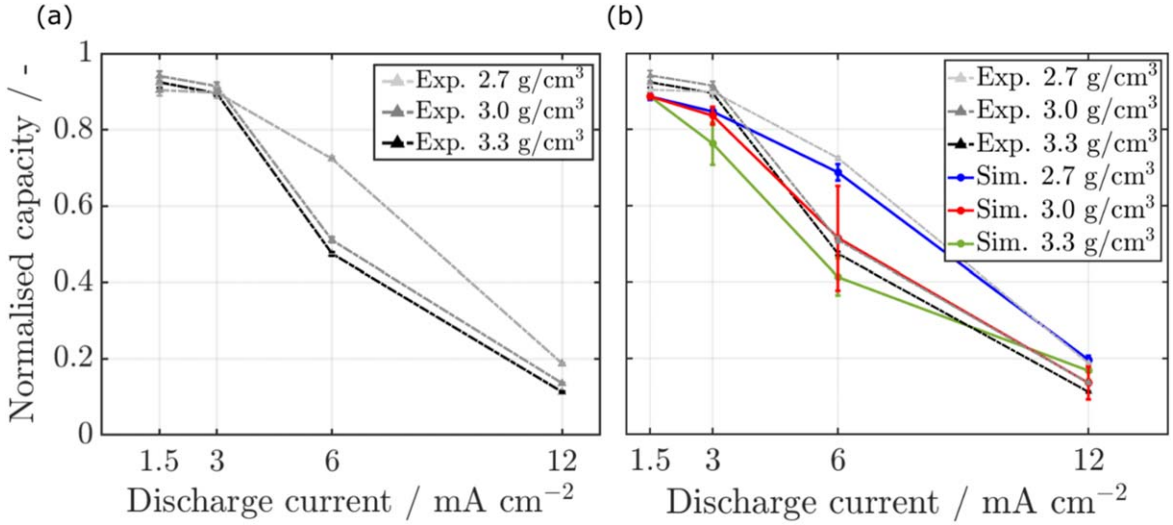

Figure 14. Plot (a) shows the end-of-discharge (at 3.0 V) capacity for measurements (in gray) at three different electrode densities for varying discharge currents. Plot (b) shows the average end-of-discharge (at 3.0 V) simulated capacity at all electrode densities for the "Combined" scenario at all discharge currents. The end capacities for the experiments and simulations were normalised to their theoretical capacity value. The standard deviation arises from considering all cutouts for each electrode. The abbreviations "Exp." and "Sim." stand for experimental data and simulation results, respectively.

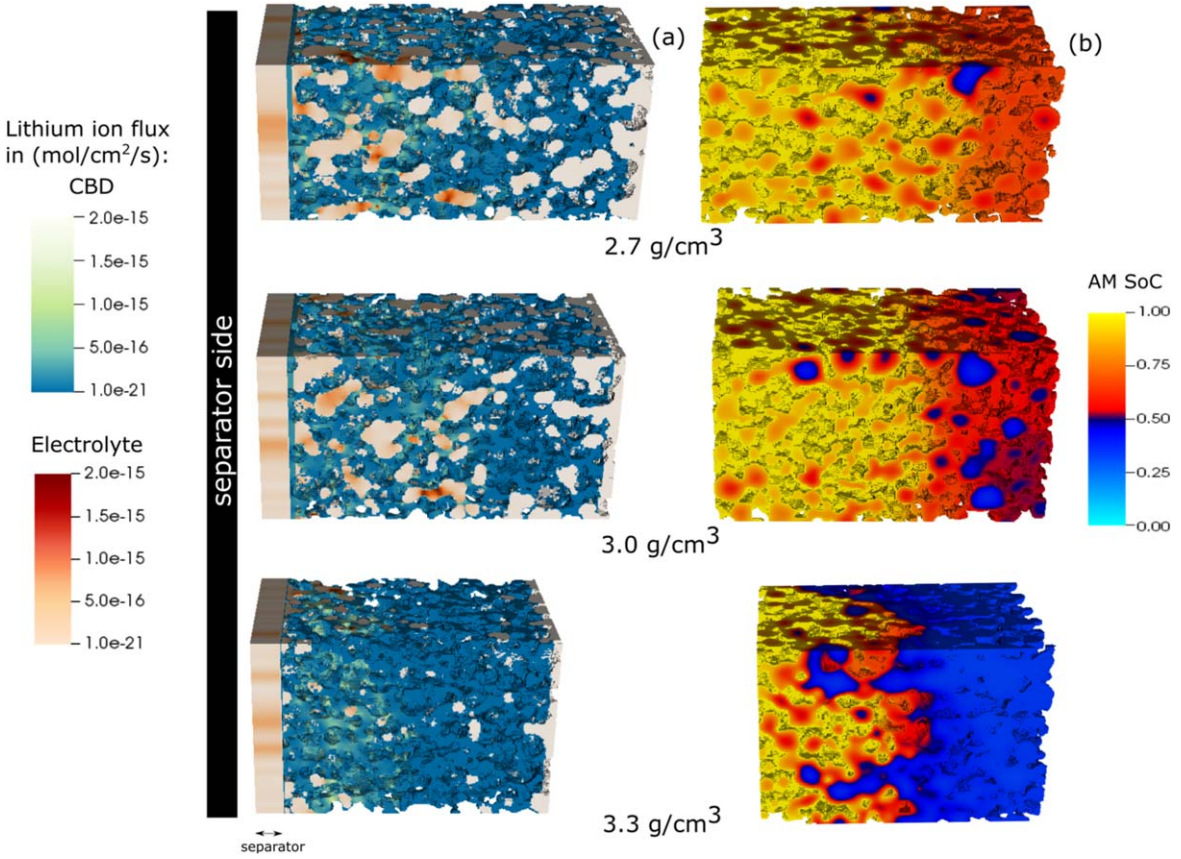

Figure 15. 3D material distribution in "Combined" case electrodes with densities of 2.7, 3.0 and 3.3 g cm^{-3} at the lower cutoff (3.0 V) of a lithiation simulation with 6 mA/cm2 constant current. (a) Flux of lithium-ion in the CBD (shown by the orange color scale) and mesoporous space (blue color scale). (b) Cathode AM state-of-charge (SoC) representing the normalized lithium distribution in an electrode with varying densities. The separator is on the left hand side of the 3D distribution in each panel and the current collector is to the right.

at the other densities (see Supporting Information Section 4.2.2.). This could be an advantageous side-effect of calendering the electrodes, rendering the resistance to ion flux at the separator smaller. It is, therefore, critical to resolve the electrode microstructure for the simulations, and consider the effects of electrode processing steps on the local CBD properties.

Summary and Conclusions

In this paper, we investigate the effect of an inhomogeneous CBD distribution on electrode impedance and rate performance. Such inhomogeneities have been reported for high drying rates, especially in electrodes with high areal density. An indicative feature for inhomogeneities in the electrode microstructure is an additional semi-circle which is observed at high frequencies in the impedance spectra of symmetric cells under blocking conditions. Although semicircular in shape, characteristic frequencies of this feature are higher compared to those of charge transfer processes. In our study, we investigate different scenarios of an inhomogeneous binder distribution for different electrode densities. In particular, we found that both a dense layer of CBD close to the separator, and a CBD-free layer close to the CC are able to reproduce the semi-circle in the impedance. Considering the two cases provides the best match to the experimental data and is in-line with common concepts of binder migration. In addition to the impedance spectra, we simulate lithiation of the electrodes in a half-cell configuration. These simulations clearly show that dense layers of CBD have a detrimental effect on discharge capacity. The scenario reproducing the symmetric impedance spectra with a dense layer of CBD close to the separator shows very poor discharge performance. On the other hand, scenario with only a CBD-absent layer close to the current collector overestimates the discharge capacity significantly. Again, the best match with the experimental data was found for an electrode bearing the two effects. Therefore, we can show that combining information from symmetric cell impedance spectra and half-cell rate tests provides significant insights on passive material distribution and thus, the rate limiting processes. Additionally, we could also shed light on the importance of choosing process parameters preventing the migration of the CBD to the surface, since it is much more detrimental to performance from an electrochemical perspective, compared to CBD depleted layers at the current collector.

Acknowledgments

This work has been funded by the "Bundesministerium für Bildung und Forschung" within the project HiStructures under the reference Nos. 03XP0243A, 03XP0243D and 03XP0243E. Particularly the work of Lea Kremer for preparing the electrodes and contributing the related data, and Daniel Westhoff for segmenting the 3D image data obtained by synchrotron tomography. The authors also acknowledge the funding and support by the German Research Foundation (DFG) within the research training group SiMET under the project number 281041241/GRK2218. And last, but not least, the state of Baden-Württemberg through bwHPC

and the German Research Foundation (DFG) through grant number INST 40/575-1 FUGG (JUSTUS 2 cluster).

ORCID

Mrudula Prasad https://orcid.org/0009-0006-9796-4632
Simon Hein https://orcid.org/0000-0002-6728-9983
Timo Danner https://orcid.org/0000-0003-2336-6059
Benedikt Prifling https://orcid.org/0000-0002-2952-0208
Rares Scurtu https://orcid.org/0000-0003-1635-4930
Alice Hoffmann https://orcid.org/0000-0003-0541-1194
André Hilger https://orcid.org/0000-0002-6454-7967
Markus Osenberg https://orcid.org/0000-0003-0836-627X
Ingo Manke https://orcid.org/0000-0001-9795-5345
Margret Wohlfahrt-Mehrens https://orcid.org/0000-0002-5118-5215
Arnulf Latz https://orcid.org/0000-0003-1449-8172

References

1. L. S. Kremer, A. Hoffmann, T. Danner, S. Hein, B. Prifling, D. Westhoff, C. Dreer, A. Latz, V. Schmidt, and M. Wohlfahrt-Mehrens, "Manufacturing process for improved ultra-thick cathodes in high-energy lithium-ion batteries." *Energy Technology*, **8**, 1900167 (2019).
2. D. Li, Q. Lv, C. Zhang, W. Zhou, H. Guo, S. Jiang, and Z. Li, "The effect of electrode thickness on the high-current discharge and long-term cycle performance of a lithium-ion battery." *Batteries*, **8**, 101 (2022).
3. M. Xu, B. Reichman, and X. Wang, "Modeling the effect of electrode thickness on the performance of lithium-ion batteries with experimental validation." *Energy*, **186**, 115864 (2019).
4. H. Zheng, J. Li, X. Song, G. Liu, and V. S. Battaglia, "A comprehensive understanding of electrode thickness effects on the electrochemical performances of Li-ion battery cathodes." *Electrochimica Acta*, **71**, 258 (2012).
5. M. Indrikova, S. Grunwald, F. Golks, A. Netz, B. Westphal, and A. Kwade, "The morphology of battery electrodes with the focus of the conductive additives paths." *J. Electrochem. Soc.*, **162**, A2021 (2015).
6. B. Lestriez, "Functions of polymers in composite electrodes of lithium ion batteries." *Comptes Rendus Chimie*, **13**, 1341 (2010).
7. J. Chen, J. Liu, Y. Qi, T. Sun, and X. Li, "Unveiling the roles of binder in the mechanical integrity of electrodes for lithium-ion batteries." *J. Electrochem. Soc.*, **160**, A1502 (2013).
8. J. Entwistle, R. Ge, K. Pardikar, R. Smith, and D. Cumming, "Carbon binder domain networks and electrical conductivity in lithium-ion battery electrodes: a critical review." *Renew. Sustain. Energy Rev.*, **166**, 112624 (2022).
9. M. Lain and E. Kendrick, "Understanding the limitations of lithium ion batteries at high rates." *Journal of Power Sources*, **493**, 229690 (2021).
10. F. Jiang and P. Peng, "Elucidating the performance limitations of lithium-ion batteries due to species and charge transport through five characteristic parameters." *Sci. Rep.*, **6**, 32639 (2016).
11. L. Rao, X. Jiao, C.-Y. Yu, A. Schmidt, C. O'Meara, J. Seidt, J. R. Sayre, Y. M. Khalifa, and J.-H. Kim, "Multifunctional composite binder for thick high-voltage cathodes in lithium-ion batteries." *ACS Applied Materials & Interfaces*, **14**, 861 (2022).
12. A. Hoffmann, E. A. Heider, C. Dreer, C. Pfeifer, and M. Wohlfahrt-Mehrens, "Influence of the mixing and dispersing process on the slurry properties and the microstructure and performance of ultrathick cathodes for lithium-ion batteries." *Energy Technology*, **11**, 2200484 (2023).
13. J. K. Mayer, L. Almar, E. Asylbekov, W. Haselrieder, A. Kwade, A. Weber, and H. Nirschl, "Influence of the carbon black dispersing process on the microstructure and performance of Li-ion battery cathodes." *Energy Technology*, **8**, 1900161 (2020).
14. J. K. Mayer, H. Bockholt, and A. Kwade, "Inner carbon black porosity as characteristic parameter for the microstructure of lithium-ion electrodes and its effect on physical and electrochemical properties." *Journal of Power Sources*, **529**, 231259 (2022).
15. G. Liu, H. Zheng, S. Kim, Y. Deng, A. M. Minor, X. Song, and V. S. Battaglia, "Effects of various conductive additive and polymeric binder contents on the performance of a lithium-ion composite cathode." *J. Electrochem. Soc.*, **155**, A887 (2008).
16. M. Nikpour, B. Liu, P. Minson, Z. Hillman, B. A. Mazzeo, and D. R. Wheeler, "Li-ion electrode microstructure evolution during drying and calendering." *Batteries*, **8**, 107 (2022).
17. S. Jaiser, M. Müller, M. Baunach, W. Bauer, P. Scharfer, and W. Schabel, "Investigation of film solidification and binder migration during drying of Li-ion battery anodes." *Journal of Power Sources*, **318**, 210 (2016).
18. Y. Su, K. Zhou, Y. Yuan, W. Liu, and Y. Deng, "Study on prediction of binder distribution in the drying process of the coated web of positive electrode for lithium ion battery." *IOP Conference Series: Materials Science and Engineering*, **793**, 012025 (2020).
19. J. Landesfeind, A. Eldiven, and H. A. Gasteiger, "Influence of the binder on lithium ion battery electrode tortuosity and performance." *J. Electrochem. Soc.*, **165**, A1122 (2018).
20. H. Wiese and K. Weil, "An efficient Fourier transform algorithm for frequency domains of several decades using logarithmically spaced time samples." *IEEE Transactions on Acoustics, Speech, and Signal Processing*, **36**, 1096 (1988).
21. M. Doyle, J. P. Meyers, and J. Newman, "Computer simulations of the impedance response of lithium rechargeable batteries." *J. Electrochem. Soc.*, **147**, 99 (2000).
22. C. Chen, J. Liu, and K. Amine, "Symmetric cell approach and impedance spectroscopy of high power lithium-ion batteries." *Journal of Power Sources*, **96**, 321 (2001).
23. N. Ogihara, S. Kawauchi, C. Okuda, Y. Itou, Y. Takeuchi, and Y. Ukyo, "Theoretical and experimental analysis of porous electrodes for lithium-ion batteries by electrochemical impedance spectroscopy using a symmetric cell." *J. Electrochem. Soc.*, **159**, A1034 (2012).
24. D. W. Dees, D. P. Abraham, W. Lu, K. G. Gallagher, M. Bettge, and A. N. Jansen, "Electrochemical modeling and performance of a lithium- and manganese-rich layered transition-metal oxide positive electrode." *J. Electrochem. Soc.*, **162**, A559 (2015).
25. M. Schönleber, C. Uhlmann, P. Braun, A. Weber, and E. Ivers-Tiffée, "A consistent derivation of the impedance of a lithium-ion battery electrode and its dependency on the state-of-charge." *Electrochimica Acta*, **243**, 250 (2017).
26. S. Gantenbein, M. Weiss, and E. Ivers-Tiffée, "Impedance based time-domain modeling of lithium-ion batteries: Part I." *Journal of Power Sources*, **379**, 317 (2018).
27. R. Morasch, J. Landesfeind, B. Suthar, and H. A. Gasteiger, "Detection of binder gradients using impedance spectroscopy and their influence on the tortuosity of Li-ion battery graphite electrodes." *J. Electrochem. Soc.*, **165**, A3459 (2018).
28. T.-T. Nguyen, "The study of the correlation between the microstructural properties and the electrochemical performance of the Li-ion battery high-energy-density positive electrode." *Doctoral Thesis*, Université de Picardie Jules Verne (2021).
29. J. Landesfeind, M. Ebner, A. Eldiven, V. Wood, and H. A. Gasteiger, "Tortuosity of battery electrodes: Validation of impedance-derived values and critical comparison with 3D tomography." *J. Electrochem. Soc.*, **165**, A469 (2018).
30. J. E. Vogel, M. M. Forouzan, E. E. Hardy, S. T. Crawford, D. R. Wheeler, and B. A. Mazzeo, "Electrode microstructure controls localized electronic impedance in Li-ion batteries." *Electrochimica Acta*, **297**, 820 (2019).
31. S. Hein et al., "Influence of conductive additives and binder on the impedance of lithium-ion battery electrodes: effect of morphology." *J. Electrochem. Soc.*, **167**, 013546 (2020).
32. J. Landesfeind, J. Hattendorff, A. Ehrl, W. A. Wall, and H. A. Gasteiger, "Tortuosity determination of battery electrodes and separators by impedance spectroscopy." *J. Electrochem. Soc.*, **163**, A1373 (2016).
33. A. Shodiev, E. N. Primo, M. Chouchane, T. Lombardo, A. C. Ngandjong, A. Rucci, and A. A. Franco, "4D-resolved physical model for electrochemical impedance spectroscopy of $Li(Ni_{1-x-y}\ Mn_x\ Co_y)O_2$ -based cathodes in symmetric cells: Consequences in tortuosity calculations." *Journal of Power Sources*, **454**, 227871 (2020).
34. M. Gaberscek, J. Moskon, B. Erjavec, R. Dominko, and J. Jamnik, "The importance of interphase contacts in Li ion electrodes: The meaning of the high−frequency impedance arc." *Electrochem. Solid−State Lett.*, **11**, A170 (2008).
35. R. Kant and M. B. Singh, "Theory of the electrochemical impedance of mesostructured electrodes embedded with heterogeneous micropores." *The Journal of Physical Chemistry C*, **121**, 7164 (2017).
36. K. Miyasaka, K. Watanabe, E. Jojima, H. Aida, M. Sumita, and K. Ishikawa, "Electrical conductivity of carbon−polymer composites as a function of carbon content." *J. Mater. Sci.*, **17**, 1610 (1982).
37. B. L. Trembacki, A. N. Mistry, D. R. Noble, M. E. Ferraro, P. P. Mukherjee, and S. A. Roberts, "Mesoscale analysis of conductive binder domain morphology in lithium−ion battery electrodes." *J. Electrochem. Soc.*, **165**, E725 (2018).
38. R. Dominko, M. Gaberscek, J. Drofenik, M. Bele, S. Pejovnik, and J. Jamnik, "The role of carbon black distribution in cathodes for Li ion batteries." *Journal of Power Sources*, **119**, 770 (2003).
39. S. Liu, X. Zeng, D. Liu, S. Wang, L. Zhang, R. Zhao, F. Kang, and B. Li, "Understanding the conductive carbon additive on electrode/electrolyte interface formation in lithium−ion batteries via in situ scanning electrochemical microscopy." *Frontiers in Chemistry*, **8**, 114 (2020).
40. Y. K. Lee, "The effect of active material, conductive additives, and binder in a cathode composite electrode on battery performance." *Energies*, **12**, 658 (2019).
41. F. Jeschull, J. Maibach, K. Edström, and D. Brandell, "On the electrochemical properties and interphase composition of graphite: PVdF−HFP electrodes in dependence of binder content." *J. Electrochem. Soc.*, **164**, A1765 (2017).
42. G. Liu, H. Zheng, S. Kim, Y. Deng, A. M. Minor, X. Song, and V. S. Battaglia, "Effects of various conductive additive and polymeric binder contents on the performance of a lithium−ion composite cathode." *J. Electrochem. Soc.*, **155**, A887 (2008).
43. T. Knorr, S. Hein, B. Prifling, M. Neumann, T. Danner, V. Schmidt, and A. Latz, "Simulation−based and data−driven techniques for quantifying the influence of the carbon binder domain on electrochemical properties of Li−ion batteries." *Energies*, **15**, 7821 (2022).
44. A. Mistry, S. Trask, A. Dunlop, G. Jeka, B. Polzin, P. P. Mukherjee, and V. Srinivasan, "Quantifying negative effects of carbon−binder networks from electrochemical performance of porous Li−ion electrodes." *J. Electrochem. Soc.*, **168**, 070536 (2021).
45. B. Prifling et al., "Quantitative comparison of different approaches for reconstructing the carbon−binder domain from tomographic image data of cathodes in lithium−ion batteries and its influence on electrochemical properties." *Energy Technology*, **11**, 2200784 (2023).

46. F. Boso, W. Li, K. Um, and D. M. Tartakovsky, "Impact of carbon binder domain on the performance of lithium−metal batteries." *J. Electrochem. Soc.*, **169**, 100550 (2022).
47. A. Chauhan, E. Asylbekov, S. Kespe, and H. Nirschl, "Influence of carbon binder domain on the performance of lithium−ion batteries: impact of size and fractal dimension." *Electrochemical Science Advances*, **3**, e2100151 (2023).
48. L. Zielke, T. Hutzenlaub, D. R. Wheeler, I. Manke, T. Arlt, N. Paust, R. Zengerle, and S. Thiele, "A combination of X−Ray tomography and carbon binder modeling: Reconstructing the three phases of $LiCoO_2$ Li-ion battery cathodes." *Adv. Energy Mater.*, **4**, 2 (2014).
49. A. Li, J. L. Hempel, M. P. Balogh, Y. −T. Cheng, and A. I. Taub, "Effect of binder content on silicon microparticle anodes for lithium−ion batteries." *J. Electrochem. Soc.*, **170**, 010533 (2023).
50. A. Latz and J. Zausch, "Thermodynamic consistent transport theory of Li−ion batteries." *Journal of Power Sources*, **196**, 3296 (2011).
51. A. Latz and J. Zausch, "Multiscale modeling of lithium ion batteries: thermal aspects." *Beilstein Journal of Nanotechnology*, **6**, 987 (2015).
52. A. H. Wiedemann, G. M. Goldin, S. A. Barnett, H. Zhu, and R. J. Kee, "Effects of three−dimensional cathode microstructure on the performance of lithium−ion battery cathodes." *Electrochimica Acta*, **88**, 580 (2013).
53. J. Feinauer, T. Brereton, A. Spettl, M. Weber, I. Manke, and V. Schmidt, "Stochastic 3D modeling of the microstructure of lithium−ion battery anodes via Gaussian random fields on the sphere." *Comput. Mater. Sci.*, **109**, 137 (2015).
54. W. Görner, M. P. Hentschel, B. R. Müller, H. Riesemeier, M. Krumrey, G. Ulm, W. Diete, U. Klein, and R. Frahm, "BAMline: The first hard X−ray beamline at BESSY II." *Nuclear Instruments and Methods in Physics Research, Section A: Accelerators, Spectrometers, Detectors and Associated Equipment*, **467**, 703 (2001).
55. Fraunhofer Institute for Industrial Mathematics (ITWM), BEST −Battery and Electrochemistry Simulation Tool (2020). http://itwm.fraunhofer.de/best.
56. A. Nyman, M. Behm, and G. Lindbergh, "Electrochemical characterisation and modelling of the mass transport phenomena in $LiPF_6$-EC-EMC electrolyte." *Electrochimica Acta*, **53**, 6356 (2008).
57. S. G. Meibuhr, "Electrode studies in nonaqueous electrolytes." *J. Electrochem. Soc.*, **117**, 56 (1970).
58. R. Amin and Y. −M. Chiang, "Characterization of electronic and ionic transport in Li_{1-x} $Ni_{0.33}$ $Mn_{0.33}$ $Co_{0.33}$ O_2 (NMC333) and Li_{1-x} $Ni_{0.50}$ $Mn_{0.20}Co_{0.30}O_2$ (NMC523) as a function of Li content." *J. Electrochem. Soc.*, **163**, A1512 (2016).
59. T. Danner, M. Singh, S. Hein, J. Kaiser, H. Hahn, and A. Latz, "Thick electrodes for Li-ion batteries: A model based analysis." *Journal of Power Sources*, **334**, 191 (2016).
60. W. G. Bessler, "Rapid impedance modeling via potential step and current relaxation simulations." *J. Electrochem. Soc.*, **154**, B1186 (2007).
61. J. Ohser and F. Mücklich, *Statistical Analysis of Microstructures in Materials Science* (Wiley) (2000).